nature materials

SUPPLEMENTARY INFORMATION
https://doi.org/10.1038/s41563-018-0236-9

In the format provided by the authors and unedited.

Long spin coherence length and bulk-like spin–orbit torque in ferrimagnetic multilayers

Jiawei Yu[1], Do Bang[2,3,8], Rahul Mishra[1,8], Rajagopalan Ramaswamy[1], Jung Hyun Oh[4], Hyeon-Jong Park[5], Yunboo Jeong[6], Pham Van Thach[2,3], Dong-Kyu Lee[4], Gyungchoon Go[4], Seo-Won Lee[4], Yi Wang[1], Shuyuan Shi[1], Xuepeng Qiu[7], Hiroyuki Awano[2], Kyung-Jin Lee[4,5,6]* and Hyunsoo Yang[1]*

[1]Department of Electrical and Computer Engineering, National University of Singapore, Singapore, Singapore. [2]Toyota Technological Institute, Tempaku, Nagoya, Japan. [3]Institute of Materials Science, Vietnam Academy of Science and Technology, Hanoi, Vietnam. [4]Department of Materials Science and Engineering, Korea University, Seoul, Korea. [5]KU-KIST Graduate School of Converging Science and Technology, Korea University, Seoul, Korea. [6]Department of Semiconductor Systems Engineering, Korea University, Seoul, Korea. [7]Shanghai Key Laboratory of Special Artificial Macrostructure Materials and Technology and School of Physics Science and Engineering, Tongji University, Shanghai, China. [8]These authors contributed equally: Do Bang, Rahul Mishra
*e-mail: kj_lee@korea.ac.kr; eleyang@nus.edu.sg

Supplementary Information

Long spin coherence length and bulk-like spin-orbit torque in ferrimagnetic multilayers

Jiawei Yu[1], Do Bang[2,3,8], Rahul Mishra[1,8], Rajagopalan Ramaswamy[1], Jung Hyun Oh[4], Hyeon-Jong Park[5], Yunboo Jeong[6], Pham Van Thach[2,3], Dong-Kyu Lee[4], Gyungchoon Go[4], Seo-Won Lee[4], Yi Wang[1], Shuyuan Shi[1], Xuepeng Qiu[7], Hiroyuki Awano[2], Kyung-Jin Lee[4,5,6*], and Hyunsoo Yang[1*]

[1] Department of Electrical and Computer Engineering, National University of Singapore, 117576, Singapore

[2] Toyota Technological Institute, Tempaku, Nagoya 468-8511, Japan

[3] Institute of Materials Science, Vietnam Academy of Science and Technology, 18 Hoang Quoc Viet, Cau Giay, Hanoi, Vietnam

[4] Department of Materials Science and Engineering, Korea University, Seoul 02841, Korea

[5] KU-KIST Graduate School of Conversing Science and Technology, Korea University, Seoul 02841, Korea

[6] Department of Semiconductor Systems Engineering, Korea University, Seoul 02841, Korea

[7] Shanghai Key Laboratory of Special Artificial Macrostructure Materials and Technology and School of Physics Science and Engineering, Tongji University, Shanghai 200092, China

[8] These authors contributed equally to this work.

*e-mail: kj_lee@korea.ac.kr, eleyang@nus.edu.sg

Supplementary Note 1. Theoretical modeling

In this section, we show a model calculation result of non-equilibrium spin density induced by the spin Hall effect (SHE) of a heavy metal (HM) layer in contact with a magnetic layer. We note that our model treats the SHE of a HM in a phenomenological way and thus cannot capture details of the spin Hall physics. However, it correctly describes the spin polarization carried by the SHE-induced spin current, which is sufficient for our purpose as we investigate how a transverse spin current flowing perpendicular to the electric field is absorbed by a magnetic layer.

We consider the device with the Hamiltonian, given as

$$H = \frac{(\boldsymbol{p}-q\boldsymbol{A})^2}{2m} + \Delta_{ex}\vec{\sigma}\cdot\boldsymbol{m}, \tag{1}$$

where $q = -|e|$ is the electron charge, $\boldsymbol{A}$ is a vector potential for an electric field, $\vec{\sigma}$ is the Pauli matrix, and Δ_{ex} is an exchange energy that is finite for a magnetic material and zero for a heavy metal. We model the vector potential as

$$\boldsymbol{A} = A_0(t)\hat{x} + \alpha_{SH}\vec{\sigma}\times A_0(t)\hat{x}, \tag{2}$$

under an alternating electric field applied along the *x*-direction as $A_0(t) = -\frac{E_0}{\omega}\sin(\omega t)$ with an electric field strength E_0. The first term describes the vector potential associated with the applied electric field and the second term denotes the vector potential with the effective field direction that is perpendicular to both the applied electric field and the electronic spin. We introduce the second term in a phenomenological way to mimic the SHE whose symmetry requires that a spin polarization is transverse to both an electric field and a spin current flow[1,2]. The spin Hall coefficient α_{SH} is assumed to be finite in a heavy metal.

For a given Hamiltonian, a non-equilibrium spin density is calculated through a lesser Green function of the device by treating the vector potential perturbatively. A lesser Green function can be written as, under perturbation U;[3,4]

$$G^< = G^R\Sigma^< G^A = (1+G^R U)g^<(1+UG^A), \tag{3}$$

where $g^<$ is an unperturbed lesser Green function. G^R is a retarded Green function satisfying a Dyson equation,

$$G^R = g^R + g^R U G^R, \tag{4}$$

with an unperturbed Green function g^R and $G^A = [G^R]^\dagger$. By expanding G^R in a series of U and retaining the first order of U in $G^<$, we obtain the non-equilibrium spin density as,

$$\delta\boldsymbol{s} = \mathrm{Tr}\{-i\hbar\,(G^< - g^<)\vec{\sigma}\} = \int dE\left[\frac{\partial f_{FD}(E-\mu)}{\partial E}\mathrm{Tr}\{\delta\boldsymbol{N}\} + f_{FD}(E-\mu)\mathrm{Tr}\{\delta\boldsymbol{D}\}\right], \tag{5}$$

where Tr means a trace over spins. Here, $\delta\boldsymbol{N}$ and $\delta\boldsymbol{D}$ are the Fermi surface and sea contributions given by[5]

$$\delta\boldsymbol{N} = \frac{\hbar}{4\pi}\left[g^R\frac{\partial U}{\partial t}g^R + g^A\frac{\partial U}{\partial t}g^A - 2g^R\frac{\partial U}{\partial t}g^A\right], \tag{6}$$

$$\delta\boldsymbol{D} = -\frac{\hbar}{4\pi}\left[\frac{\partial g^R}{\partial E}\frac{\partial U}{\partial t}g^R - g^R\frac{\partial U}{\partial t}\frac{\partial g^R}{\partial E} + h.c\right]. \tag{7}$$

In order to calculate non-equilibrium spin density in a heavy metal/magnetic system, we consider a square lattice whose unit vectors in the *xy*-plane are given by $\vec{a}_1 = a\hat{x}$ and $\vec{a}_2 = a\hat{y}$ with a lattice constant a. As for heavy metal and ferromagnetic materials, we consider an atomic site per unit cell ($\vec{u}_1 = 0$), while, in anti-ferromagnetic materials, there are two atomic sites per unit cell, ($\vec{u}_1 = 0$ and $\vec{u}_2 = a\hat{z}$).

Then, the Hamiltonian of Eq. (1) can be written as $H = H_0 + U$ with tight-binding basis,

$$H_0 = \sum_{i,u,s}\sum_{\boldsymbol{k}}\left[\epsilon_{i,u,s}(\boldsymbol{k})a^\dagger_{ius}(\boldsymbol{k})a_{ius}(\boldsymbol{k}) - t_H a^\dagger_{i+1us}(\boldsymbol{k})a_{ius}(\boldsymbol{k}) - t_H a^\dagger_{ius}(\boldsymbol{k})a_{i-1us}(\boldsymbol{k})\right], \tag{8}$$

$$U = \sum_{i,u,s,s'}\sum_{\boldsymbol{k}}\left[U_{ss'}(\boldsymbol{k})a^\dagger_{ius}(\boldsymbol{k})a_{ius'}(\boldsymbol{k})\right], \tag{9}$$

where t_H is the hopping parameter and $\epsilon_{i,u,s}(\boldsymbol{k})$ is on-site energy at *i*-th unit cell;

$$\epsilon_{i,u,s}(\boldsymbol{k}) = -2t_H(\cos k_x a + \cos k_y a) + \Delta_{ex}\left(\delta_{u,1} - \delta_{u,2}\right)\sigma^z_{s,s}. \tag{10}$$

The perturbation potential is

$$U_{ss'}(\boldsymbol{k}) = -A_0(t)\hat{x}\cdot(\boldsymbol{J} + \alpha_{SH}\vec{\sigma}\times\boldsymbol{J})_{ss'}, \tag{11}$$

where $\boldsymbol{J}$ is a current operator,

$$\boldsymbol{J} = -\frac{|e|}{\hbar}\frac{\partial}{\partial\boldsymbol{k}}\epsilon(\boldsymbol{k}) = 2\frac{|e|}{\hbar}t_H a(\hat{x}\sin k_x a + \hat{y}\sin k_y a). \tag{12}$$

Because of $g^R(E) = [E - H_0 + i\Gamma]^{-1}$ in a matrix form with a constant line broadening Γ,[2,5] we can obtain the non-equilibrium spin density by integrating $\delta\boldsymbol{N}$ and $\delta\boldsymbol{D}$ over energy- and $\boldsymbol{k}$-space. We note that this model is too simple to capture all the details of FIMs shown in the main text. As a result, we use this model calculation to get an insight into the spin coherence length in FMs and FIMs, but do not attempt to quantitatively reproduce experimental results.

Fig. S1a shows a calculated non-equilibrium spin density carried by a spin current flowing along the *z*-axis for an isolated heavy metal (HM, e.g., Pt) layer when an electric field is applied along the *x*-axis and the level broadening Γ is 25 meV. The calculation shows that the only spin-*y* density is carried by the spin current, therefore describing the symmetry of SHE properly. In Fig. S1b, we compare the non-equilibrium spin density for M/HM bilayers for M = ferromagnet (FM), ferrimagnet (FIM), or antiferromagnet (AFM) and the magnetization **m** of M layer pointing along the z-axis. Here the direction of **m** is alternating in sub-lattices A and B for FIM and AFM. In this configuration, the x-component of non-equilibrium spin density corresponds to the anti-damping torque because the direction of anti-damping torque is $\mathbf{m} \times [\mathbf{m} \times (\mathbf{E} \times \mathbf{z})] = \mathbf{m} \times \mathbf{x}$. The right panel shows that the thickness-averaged non-equilibrium spin density $\langle s_x \rangle$ of FM/HM follows 1/thickness-dependence (thus surface-torque characteristic). On the other hand, $\langle s_x \rangle$ of FIM/HM and AFM/HM decays much slower than that of FM/HM, exhibiting the bulk-like-torque characteristic. In this plot, we note that $\langle s_x \rangle$ of AFM/HM decays due to the level broadening Γ and $\langle s_x \rangle$ of FIM/HM decays faster than that of AFM/HM due to the difference between the sub-lattice exchange interactions (Δ_A and Δ_B). These results show that the spin-orbit torque is also a surface torque for a FM, while it has features of bulk-like-torque characteristics for a FIM and AFM.

Using the same model, we compute the non-equilibrium spin density of FIMs for which we consider the thickness-dependent property variation. Compared to Fig. S1 where the *sd* exchange interactions are identical regardless of the total thickness, we assume for FIMs that the *sd* exchange interactions of two sub-layers (e.g. Δ_A for Co layer and Δ_B for Tb layer) vary with the total thickness of FIM, motivated by the experimental observation. For FIMs, we compute three cases: FIM multilayer (the alternation of two sub-layers is perfectly periodic), FIM alloy1 (the alternation is fully random), and FIM alloy2 (the alternation is partially random: 8 out of 52 layers are randomly mixed). For all three cases of FIM, we use the (Δ_A, Δ_B) set shown in Fig. S2a. For alloys, we average the calculation results for 20 different realizations of randomness.

Fig. S2b shows the total non-equilibrium spin density $S_x^{tot}\left(\equiv \sum_{i=1}^{N} s_x^i\right)$ as a function of t_{tot} for FM and FIMs, where s_x^i is the non-equilibrium spin density at the i^{th} layer, N is the number of atomic layers, t_{tot} (= Na) is the total thickness, and a is the thickness of an atomic layer. S_x^{tot} of FM (blue square symbols) is almost constant, reflecting the surface-torque characteristic. As the effective spin Hall angle θ_{eff} is constant for FMs, S_x^{tot} can be compared with the experimentally estimated θ_{eff} (Fig. 3c,d of the main text). On the other hand, S_x^{tot} of a FIM multilayer (red circle symbols) first increases with t_{tot}, and then decreases. This thickness-dependence for a FIM multilayer is caused by the assumed thickness-dependent exchange. We observe that the maximum S_x^{tot} occurs at a thickness different from that for the exact antiferromagnetic condition (i.e., $|\Delta_A - \Delta_B|=0$).

We note that the computation results for FIM multilayers are in qualitative agreement with the experimental ones (Fig. 3d of the main text), even though the detailed explanation is more complex and details of the FIM structure would probably play a role. The qualitative similarity between the calculated S_x^{tot} and the experimental θ_{eff} has several implications for our study. It suggests that θ_{eff} of a FIM can be larger than that of a FM, resulting from the long spin coherence length. It also suggests that the distinct thickness dependence of θ_{eff} in a FIM would originate from the intrinsic effect (i.e., long spin coherent length) combined with an extrinsic effect (i.e., thickness-dependent variation of the property). Finally, it suggests that the exchange compensation in our samples would occur near the thickness where the saturation magnetization M_S is compensated.

Fig. S2b also shows S_x^{tot} for two other cases of FIM alloy. For the FIM alloy1 where the alternation of two sub-layers is fully random, S_x^{tot} is almost constant as for a FM, indicating that the perfect disorder completely destroys the spin coherence in the bulk part of FIM and the spin torque shows the surface-torque characteristic. On the other hand, when we assume a partial randomness for the alternation (see the FIM alloy2), the "bulk-like-torque" characteristic survives at least partially.

Supplementary Note 2. Thickness-dependent variations of magnetic properties in ferromagnetic Co/Ni and ferrimagnetic Co/Tb multilayers

The saturation magnetization (M_S) of the films shown in the inset of Fig. 3c and d of the main text is obtained by the vibrating-sample magnetometer at room temperature. To obtain the depinning field H_P, the coercivity (H_C) of the device is measured under the external field at various angles (φ) with respect to the film normal. The H_C as a function of φ is fitted with $H_P/\cos\varphi$ and H_P can be obtained.

To measure the anisotropy field (H_K), an external field with a small out-of-plane tilting angle is applied to the device as shown in Fig. S3a. The equilibrium direction of the magnetization can be described as

$$H\sin(\theta-\theta_H)-H_K\sin\theta\cos\theta=0 \tag{13}$$

where H, θ, and θ_H are the external magnetic field, magnetization direction and external magnetic field direction, respectively. As $R_H = R_{AHE}\sin\theta$, where R_H is the Hall resistance and R_{AHE} is the anomalous Hall resistance with the magnetization aligned along the normal direction of the film plane. H_K can be obtained by fitting the anomalous Hall loop with Eq. (13). The representative fitting for the $[Co/Tb]_5$ device is shown in Fig. S3b.

Fig. S4 shows thickness-dependent variations of magnetic properties and switching current densities. The ferromagnetic Co/Ni multilayer shows monotonic decays of the depinning field H_P and the effective anisotropy H_K. On the other hand, the ferrimagnetic Co/Tb multilayer shows significant thickness-dependent variations in H_P and H_K, whiles it shows relatively small changes in the switching current density.

The current densities in Fig. S4e and Fig. S4f are obtained using a "one-dimensional current shunting model".[6] First, the averaged current density in the whole stack (J_{tot}) are calculated using $J_{tot} = \frac{I}{(t_{FM/FIM} + t_{HM}) \cdot w}$, where w is the device width and I is the applied current. In the second harmonic measurements, we have $I = I_{ac} / 2\sqrt{2}$, where I_{ac} is the peak to peak value of the applied ac current, whereas in the current induced switching measurements, we sweep a pulsed dc current I. $t_{FM/FIM}$ and t_{HM} are the FM (or FIM) and HM layer thicknesses, respectively. The current density in the HM layer can be expressed as $J_{HM} = \frac{1}{\rho_{HM}} \frac{t_{FM/FIM} + t_{HM}}{t_{FM/FIM}/\rho_{FM/FIM} + t_{HM}/\rho_{HM}} J_{tot}$, where $\rho_{FM/FIM}$ and ρ_{HM} are the resistivities of FM (or FIM) and HM layers, respectively. In this work, we have ρ_{HM} = 45 μΩ·cm (for 4nm-thick Pt), while ρ_{FM} and ρ_{FIM} change with the film thickness (see Fig. S9 for details).

Supplementary Note 3. Comparison of SOT effective fields in Co/Tb sample without and with a Pt layer

We experimentally check whether the pure bulk Co/Tb contributes to SOT in $[Tb/Co]_N$/Pt multilayers. Jamali *et al*.[7] reported Co/Pd bulk contribution to SOT beyond the spin Hall effect, arising from strong lattice distortions. Huang *et al*.[8] reported a non-cancellation of SOT in Co/Pt multilayers coming from the asymmetric Co/Pt and Pt/Co interfaces. We thus check the Co/Tb bulk contribution by comparing SOT from Co/Tb samples without and with the Pt layer. A reference Co/Tb sample with 5 nm SiO_2 capping and N = 7 is prepared. It must be noted that the Pt layer, which functions as a SOT source, is eliminated in this structure. Therefore, the structure is a reference system to estimate the pure Co/Tb contribution to SOT.

We first present the data from the harmonic Hall voltage measurements. The measurement results from the longitudinal configuration are shown in Fig. S5a, b for devices with and without Pt capping, respectively. The 1st harmonic voltages are shown in the insets of Fig. S5a, b, indicating perpendicular magnetization anisotropy (PMA) in both samples. For the Co/Tb sample with a SOT source (Pt capping = 2 nm, N = 5), there is a clear positive/negative peak in the 2nd harmonic voltage signal as shown in Fig. S5a, indicating a sizable SOT effective field (H_L). As for the Co/Tb without a SOT source (without Pt capping), no noticeable peak is observed as shown in Fig. S5b, indicating a negligible H_L. Therefore, we conclude that bulk Co/Tb itself cannot directly contribute to SOT.

As an independent method to check the SOT,[9] a large dc current (corresponding to a current density of 10^7 A/cm^2) is injected into the channel as shown in Fig. S6a. In order to coherently rotate the magnetization, θ is kept as 2° to assure a finite z component of the external field. As shown in Fig. S6b, in Co/Tb sample (N = 5) with Pt capping, an apparent difference between the R_H curves is observed for I_{dc} = +6 and –6 mA. The difference indicates that the dc current acts like an easy-axis effective field,[10] which assists or impedes the external field (H_z) in rotating the magnetization of the FIM layer. The effect of the dc current can be understood by the SOT theory, where the direction of anti-damping SOT field (H_L) is $(\hat{\mathbf{z}} \times \mathbf{j}) \times \hat{\mathbf{m}} = \hat{\mathbf{y}} \times \hat{\mathbf{m}}$. The H_L has a non-zero z component when $\hat{\mathbf{m}}$ is tilted in the x-direction by in-plane external field and thus behaves like an effective H_z field.[11] A considerable SOT is therefore confirmed in Co/Tb with the Pt capping layer, which agrees well with the second harmonic results as shown in Fig. S5a. As for the sample without Pt capping, R_H curves with I_{dc} = +4 and –4 mA show no difference, indicating there is no current-induced effective field from the dc current, as shown in Fig. S6c. Therefore, we confirm that Co/Tb bulk itself does not directly contribute to SOT.

We also carry out spin pumping measurements in substrate/Pt (10)/Co (25) and substrate/Tb (10)/Co (25) samples (thicknesses in nm) in order to check the spin Hall effect of Tb. In our measurements, 17 dBm microwave at 7 to 9 GHz is applied from a signal generator to the device waveguide. The results from Pt based and Tb based devices are shown in Fig. S7a and 7b, respectively. It is clear that the Pt/Co structure shows a strong inverse spin Hall signal (= V_{ISHE}/R) where R is the device resistance. On the other hand, for the Tb/Co structure, V_{ISHE}/R is negligible, indicating a negligible spin Hall angle of Tb.

Supplementary Note 4. Measurements of the anomalous Hall resistance and planar Hall resistance

The ratio of the anomalous Hall effect (AHE) and planar Hall effect (PHE) is measured in all the samples for the calculation of the SOT effective fields. The anomalous Hall resistance (R_{AHE}) is obtained by measuring the out-of-plane hysteresis loop. The result from a Co/Ni sample (N = 2) is shown in Fig. S8a as an example. The value of $2R_{\mathrm{AHE}}$ is indicated in the graph.

The planar Hall resistance (R_{PHE}) is evaluated as follows. A strong magnetic field (6 T) is applied to saturate the magnetization (M) in plane while an electrical current (I) is applied to the device channel. By rotating the sample in the film plane, the angle (θ_{IM}) between M and I changes, causing the change in the Hall resistance (R_{H}) as shown in Fig. S8b. The change of R_{H} follows the equation

$$R_H = R_{PHE}\sin\left(2\theta_{IM} + \theta_1\right) + R_0\sin\left(\theta_{IM} + \theta_2\right) + C\,. \tag{14}$$

The first term is the PHE contribution and the second term is the AHE contribution, which comes from the small out-of-plane tilting of the sample. θ_1 and θ_2 are the small offset angles which come from the measurement setup. By fitting the measurement data with Eq. (14), R_{PHE} can be extracted.

Supplementary Note 5. Resistivities of Co/Tb and Co/Ni

At first, the resistivities of different films were evaluated by fitting the conductance (1/R) versus thickness curve. As shown in Fig. S9a and Fig. S9b for Co/Tb and Co/Ni, respectively, 1/R is almost linear with t_{FIM}. However, as it is well known, the resistivity should vary with the film thickness. We therefore measured the Co/Tb and Co/Ni resistivity as a function of the film thickness as shown in Fig. S9c and Fig. S9d. All the data in Fig. 3 (main text) and Fig. S4 use the exact resistivity values of Co/Ni and Co/Tb for each thickness.

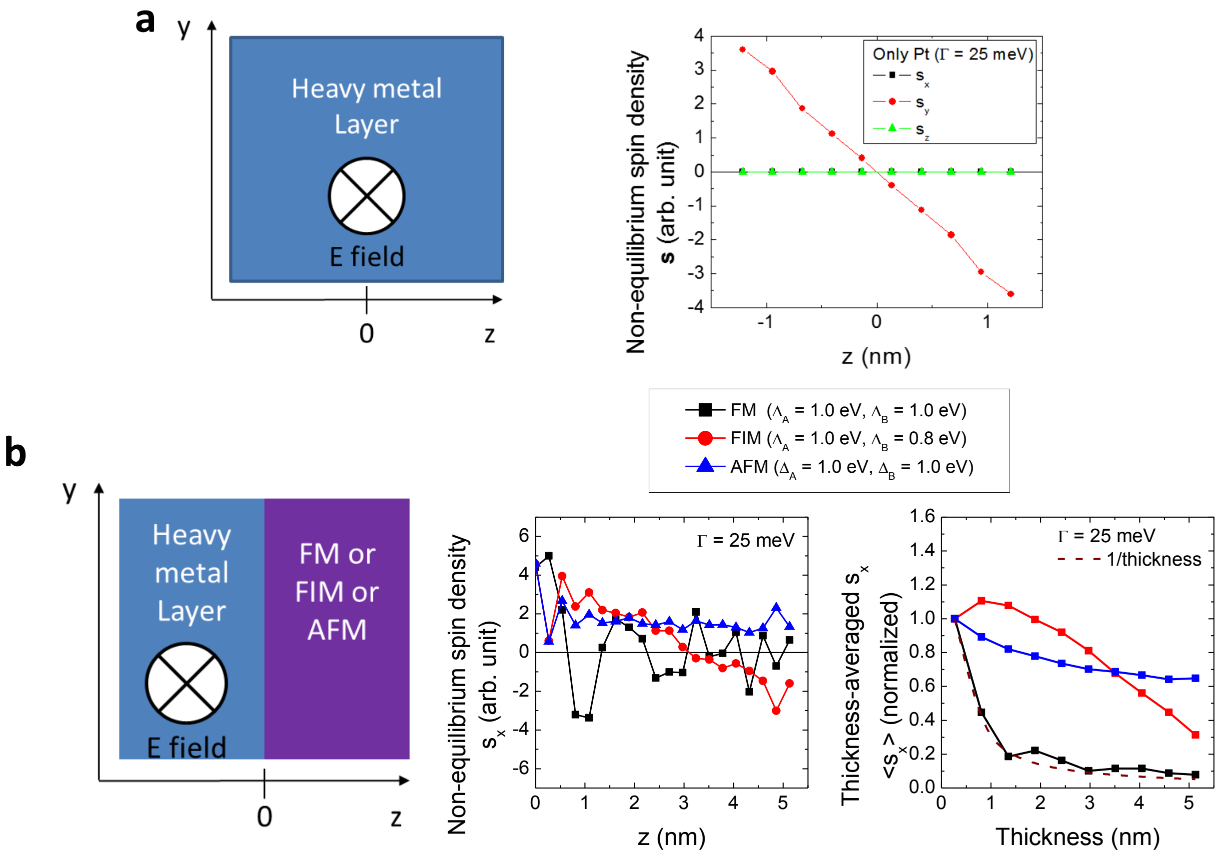

Supplementary Figure 1. Theoretical modeling. a, Non-equilibrium spin density in an isolated Pt layer. (left) A schematic illustration. (right) Distribution of component-resolved spin density along the z-axis (hopping parameter $t_H = 1.0$ eV, spin Hall coefficient $\alpha_{SH} = 0.02$, and Fermi energy $E_F = 0$ eV). **b**, Non-equilibrium spin density in a M/heavy metal bilayer [M = ferromagnet (FM), ferrimagnet (FIM), or antiferromagnet (AFM)]. (left) A schematic illustration. (center) Distribution of the *x*-component of non-equilibrium spin density s_x along the z-axis ($t_H = 1.0$ eV, $\alpha_{SH} = 0.02$, and $E_F = 0$ eV). (right) Thickness-averaged spin density $<s_x>$.

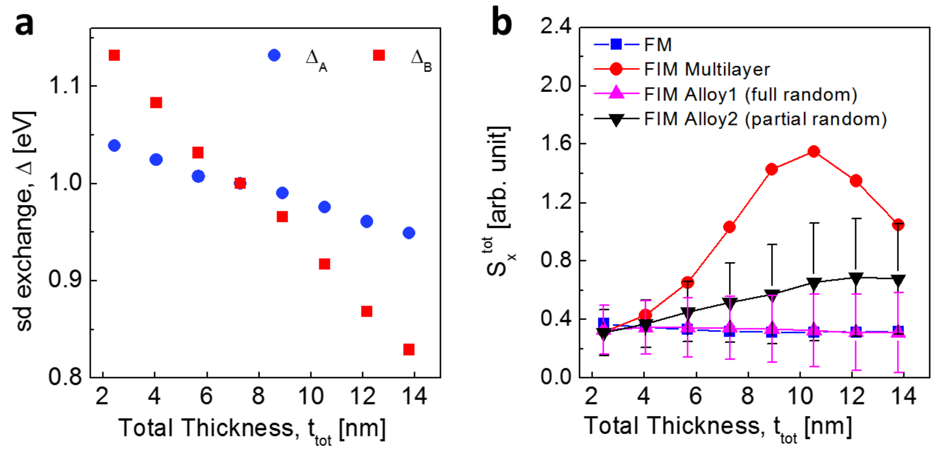

Supplementary Figure 2. Total non-equilibrium spin density calculation. a, Assumed exchange parameters (Δ_A for Co layer and Δ_B for Tb layer) for FIMs as a function of the total layer-thickness t_{tot}. (**b**) The total non-equilibrium spin density S_x^{tot} as a function of t_{tot} for FM and FIM. For FIMs, the exchange parameters (Δ_A, Δ_B) of (**a**) are used, whereas for FMs, $\Delta_A = \Delta_B = 1$ eV is used. Other common parameters: $t_H = 1.0$ eV, $\alpha_{\mathrm{SH}} = 0.02$, $E_{\mathrm{F}} = 0$ eV, the thickness of an atomic layer $a = 0.27$ nm, and broadening $\Gamma = 25$ meV. For calculation, 68,644 k-points are used.

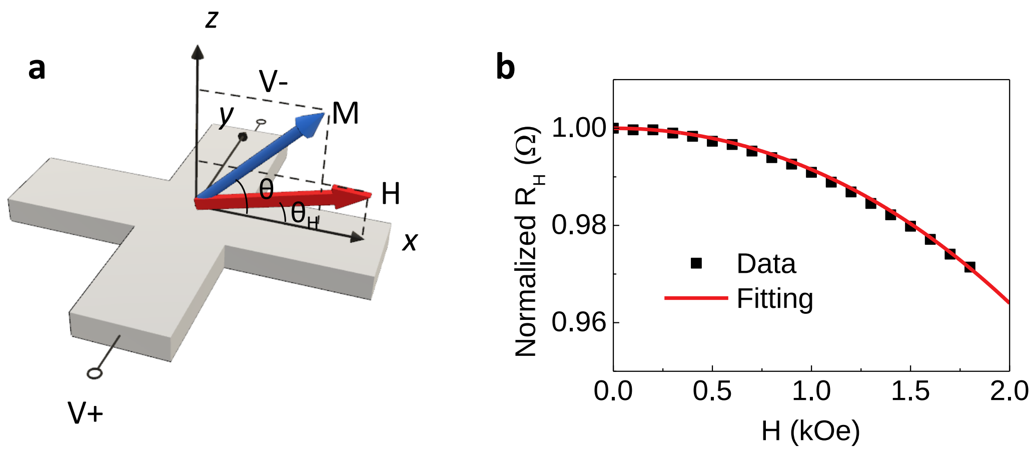

Supplementary Figure 3. Anomalous Hall measurements. Schematic of the magnetization and external magnetic field (**a**) and a representative fitting in a $[Co/Tb]_5$ device (**b**). The black dots show the normalized R_H values and the red line shows the fit.

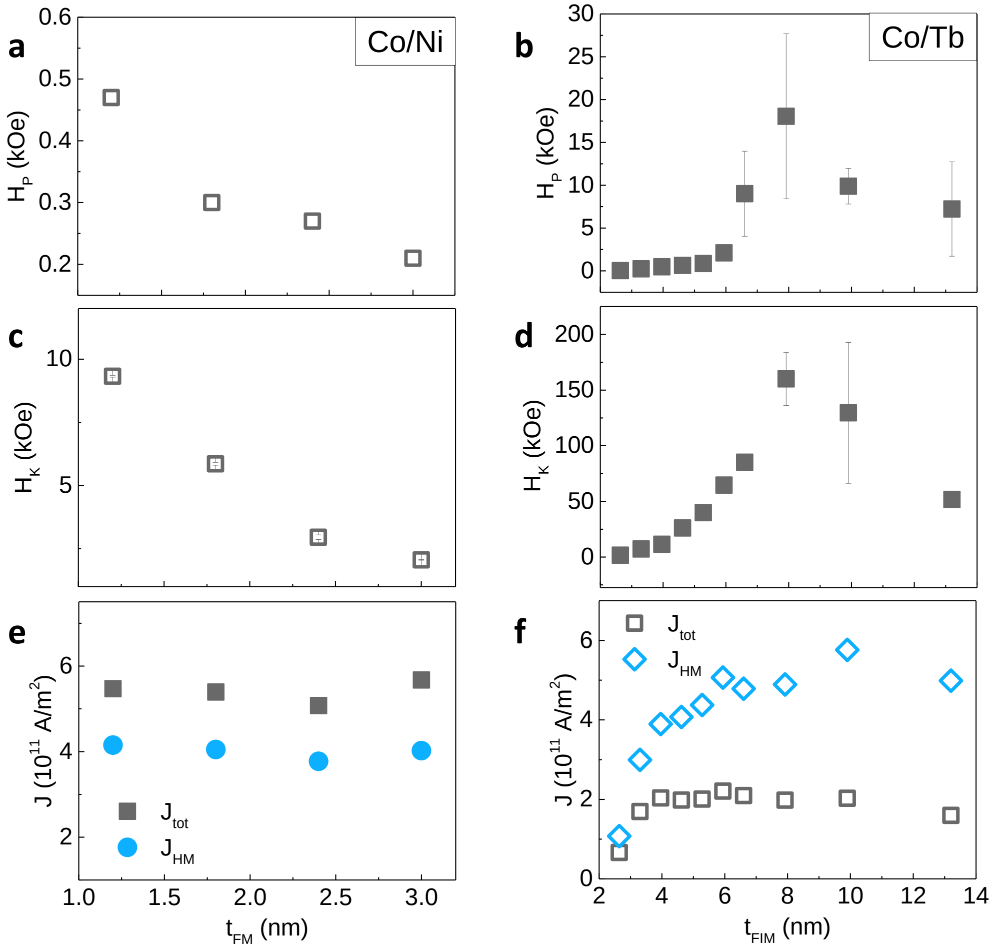

Supplementary Figure 4. Thickness-dependence of magnetic properties and switching current densities. Thickness-dependent variations of magnetic properties of Co/Ni (**a**, **c**, **e**) and Co/Tb (**b**, **d**, **f**) multilayers. **a**, **b**, Depinning field H_P. **c**, **d**, Effective anisotropy field H_K. **e**, **f**, Switching current densities estimated for the total thickness (J_{tot}) and the Pt thickness (J_{HM}).

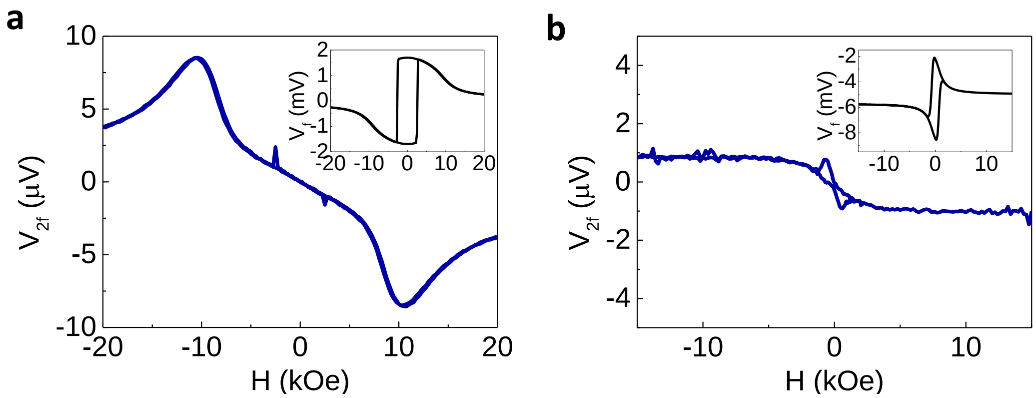

Supplementary Figure 5. Harmonic voltages from Co/Tb with and without Pt. a, **b**, The 2nd harmonic voltage signals from Co/Tb with Pt capping (**a**) and without Pt capping (**b**). Insets show the corresponding 1st harmonic voltage signals.

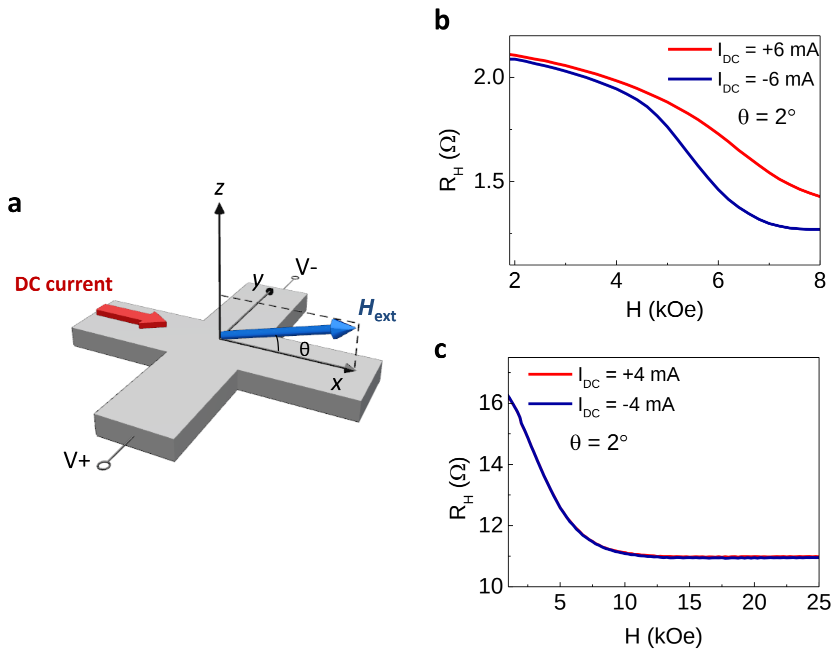

Supplementary Figure 6. Anomalous Hall resistance with dc currents. a, Schematic of the first harmonic voltage measurements with dc currents. **b**, **c**, Hall resistance (R_{H}) as a function of the applied external field with positive and negative dc currents in Co/Tb sample with Pt capping (**b**) and without Pt capping (**c**).

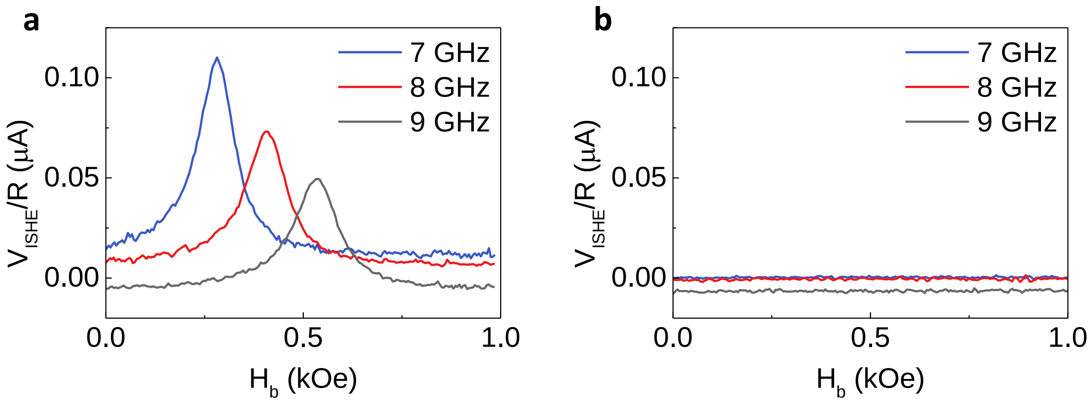

Supplementary Figure 7. Spin pumping measurements. Spin pumping signals in Pt/Co (**a**) and Tb/Co (**b**) samples.

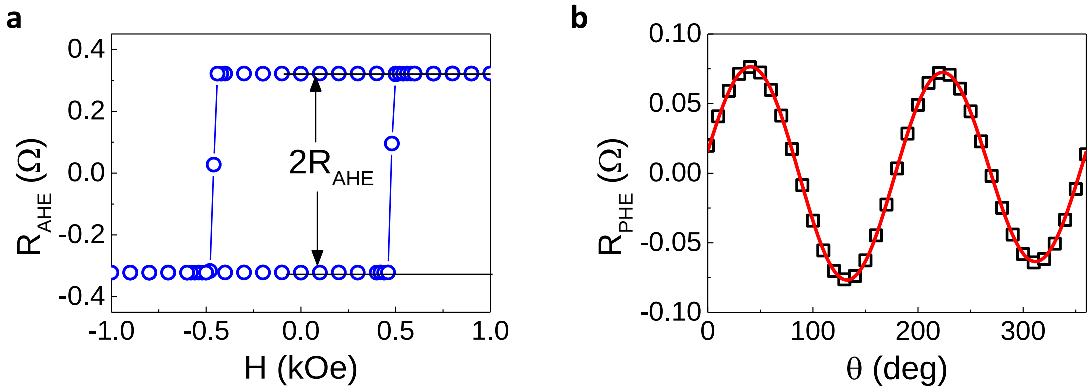

Supplementary Figure 8. Measurements of the anomalous Hall and planar Hall resistances. **a**, AHE measurement results. The Hall resistance (R_H) as a function of the applied out-of-plane magnetic field. **b**, PHE measurement results. The black symbols are the experimental data and the red line shows the fitting result.

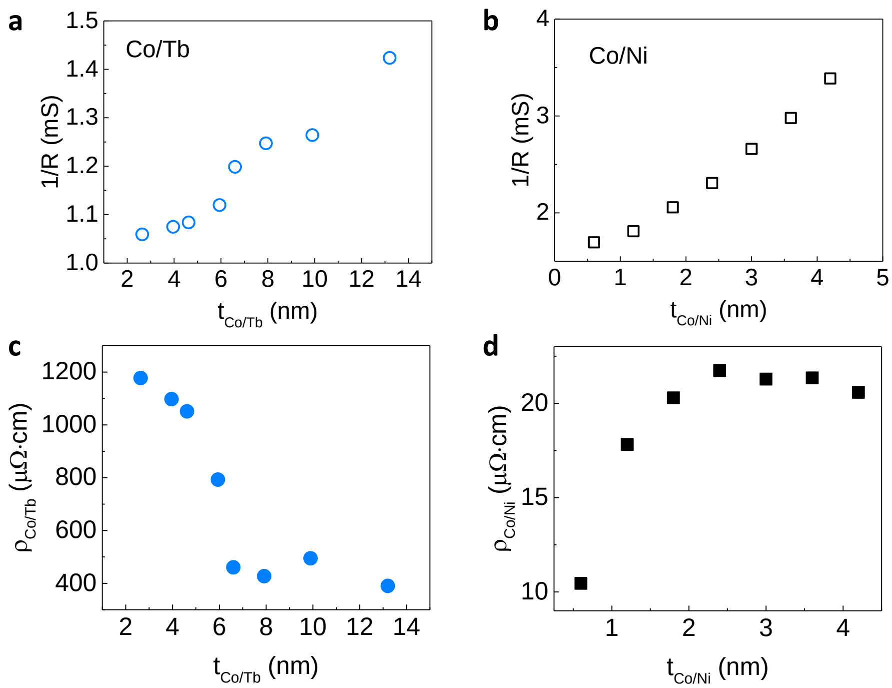

Supplementary Figure 9. Conductance and resistivity as a function of the film thickness. a, **b**, Conductance (1/R) as a function of Co/Tb and Co/Ni thickness. **c**, **d**, Resistivity as a function of Co/Tb and Co/Ni thickness.

References

1 Sinova, J., Valenzuela, S. O., Wunderlich, J., Back, C. H. & Jungwirth, T. Spin Hall effects. *Rev. Mod. Phys.* **87**, 1213-1260 (2015).

2 Tanaka, T. *et al.* Intrinsic spin Hall effect and orbital Hall effect in 4*d* and 5*d* transition metals. *Phys. Rev. B* **77**, 165117 (2008).

3 Negele, J. W. & Orland, H. Quantum many-particle systems. *Boulder, Co: Westview* (1988).

4 Datta, S. Nanoscale device modeling: the Green's function method. *Superlattice and Microstructures* **28**, 4 (2000).

5 Freimuth, F., Blügel, S. & Mokrousov, Y. Spin-orbit torques in Co/Pt(111) and Mn/W(001) magnetic bilayers from first principles. *Phys. Rev. B* **90**, 174423 (2014).

6 Yu, J., Qiu, X., Legrand, W. & Yang, H. Large spin-orbit torques in Pt/Co-Ni/W heterostructures. *Appl. Phys. Lett.* **109**, 042403 (2016).

7 Jamali, M. *et al.* Spin-Orbit Torques in Co/Pd Multilayer Nanowires. *Phys. Rev. Lett.* **111**, 246602 (2013).

8 Huang, K.-F., Wang, D.-S., Lin, H.-H. & Lai, C.-H. Engineering spin-orbit torque in Co/Pt multilayers with perpendicular magnetic anisotropy. *Appl. Phys. Lett.* **107**, 232407 (2015).

9 Liu, L. *et al.* Spin-Torque Switching with the Giant Spin Hall Effect of Tantalum. *Science* **336**, 555-558 (2012).

10 Emori, S. *et al.* Spin Hall torque magnetometry of Dzyaloshinskii domain walls. *Phys. Rev. B* **90**, 184427 (2014).

11 Lee, O. J. *et al.* Central role of domain wall depinning for perpendicular magnetization switching driven by spin torque from the spin Hall effect. *Phys. Rev. B* **89**, 024418 (2014).